Published in final edited form as:

Curr Biol. 2018 April 02; 28(7): 1039–1051.e5. doi:10.1016/j.cub.2018.02.028.

Host-Polarized Cell Growth in Animal Symbionts

Nika Pende[1], **Jinglan Wang**[2,6], **Philipp M. Weber**[1,6], **Jolanda Verheul**[2], **Erkin Kuru**[3], **Simon K.-M.R. Rittmann**[1], **Nikolaus Leisch**[1], **Michael S. VanNieuwenhze**[4], **Yves V. Brun**[5], **Tanneke den Blaauwen**[2,7], and **Silvia Bulgheresi**[1,7,8,*]

[1]University of Vienna, Department of Ecogenomics and Systems Biology, Archaeal Biology and Ecogenomics Division, Althanstrasse 14, 1090 Vienna, Austria [2]Bacterial Cell Biology and Physiology Swammerdam Institute for Life Sciences, University of Amsterdam, De Boelelaan 1108, 1081 Amsterdam, the Netherlands [3]Department of Genetics, Harvard Medical School NRB, 77 Avenue Louis Pasteur, Boston, MA, USA [4]Department of Chemistry, Indiana University, Bloomington, IN, USA [5]Department of Biology, Indiana University, Bloomington, IN, USA [6]These authors contributed equally [7]These authors contributed equally [8]Lead Contact

SUMMARY

To determine the fundamentals of cell growth, we must extend cell biological studies to non-model organisms. Here, we investigated the growth modes of the only two rods known to widen instead of elongating, *Candidatus* Thiosymbion oneisti and Thiosymbion hypermnestrae. These bacteria are attached by one pole to the surface of their respective nematode hosts. By incubating live *Ca*. T. oneisti and T. hypermnestrae with a peptidoglycan metabolic probe, we observed that the insertion of new cell wall starts at the poles and proceeds inward, concomitantly with FtsZ-based membrane constriction. Remarkably, in *Ca*. T. hypermnestrae, the proximal, animal-attached pole grows before the distal, free pole, indicating that the peptidoglycan synthesis machinery is host oriented. Immunostaining of the symbionts with an antibody against the actin homolog MreB revealed that it was arranged medially—that is, parallel to the cell long axis—throughout the symbiont life cycle. Given that depolymerization of MreB abolished newly synthesized peptidoglycan insertion and impaired divisome assembly, we conclude that MreB function is required for symbiont widening and division. In conclusion, our data invoke a reassessment of the localization and function of the bacterial actin homolog.

*Correspondence: silvia.bulgheresi@univie.ac.at.

AUTHOR CONTRIBUTIONS

N.P. did most of the experiments and display items and commented on the manuscript; J.W. did experiments; P.M.W. did experiments and display items and commented on the manuscript; J.V. did preliminary experiments; E.K. contributed to experimental design, did preliminary experiments, and commented on the manuscript; S.K.-M.R.R. did statistical analysis and commented on the manuscript; N.L. did preliminary experiments and commented on the manuscript; M.S.V. synthesized and provided peptidoglycan metabolic probes; Y.V.B. contributed to experimental design and commented on the manuscript; T.d.B. contributed to experimental design and results analysis and commented on the manuscript; and S.B. conceived the work, provided most of the funding, and wrote the manuscript.

SUPPLEMENTAL INFORMATION

Supplemental Information includes seven figures, four tables, and three movies and can be found with this article online at https://doi.org/10.1016/j.cub.2018.02.028.

DECLARATION OF INTERESTS

The authors declare no competing interests.

Graphical Abstract

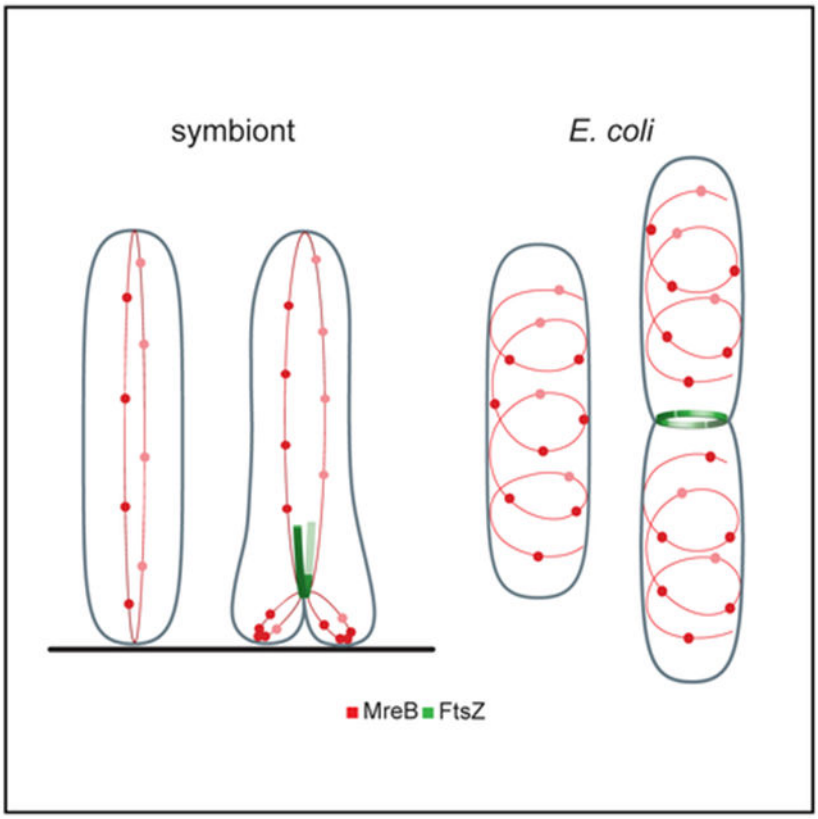

In Brief

Pende et al. show that cell growth is host oriented in two marine nematode-attached bacteria. In contrast to what is observed in model rods, the actin homolog MreB of the symbionts is arranged parallel to the cell long axis throughout the cell cycle. This medial MreB ring is essential for symbiont growth and division.

INTRODUCTION

Investigations of micro-organisms with non-canonical growth modes are necessary to identify the conserved mechanisms underlying bacterial cell proliferation. *Candidatus* Thiosymbion oneisti and *Candidatus* T. hypermnestrae form virtually pure cultures on the surface of their respective nematode hosts, *Laxus oneistus* [1] and *Robbea hypermnestra* [2]. More precisely, each rod is attached by one pole (the proximal pole) to the host so that its long axis is perpendicular to the host surface. As a result, the bacterial coat looks like a palisade. Once extracted from their natural habitat (tropical, shallow water sediment), symbiotic nematodes can be maintained in seawater-filled dishes. However, *Ca.* Thiosymbion oneisti and T. hypermnestrae cannot be grown in culture without their hosts, and no genetic tools are available to study them. Despite their relatively poor experimental tractability, we showed the reproductive mode of these *Gammaproteobacteria* to be unique, as they are the only rods known to widen and to undergo FtsZ-based longitudinal fission [3,

4]. We hypothesized that longitudinal fission might require the evolution of a special cell growth mode, as building a whole new lateral side is mechanistically more challenging than building a new pole.

In many taxa, maintenance of the rod shape itself requires at least two well-studied modes of growth: incorporation of peptidoglycan (PG) along the sidewalls (lateral elongation) and the generation of nascent poles (septation). In these canonical cases, which are exemplified by the model organisms *Escherichia coli* and *Bacillus subtilis*, material at the poles remains inert, with no evidence of new PG incorporation or turnover [5-8]. In model rods, the protein systems mediating lateral elongation and septation—the elongasome and the divisome—are genetically different. However, they both position functionally similar PG modification and synthesis machineries: the elongasome inserts new PG along the length of the rod during growth, and the divisome completes the steps of constriction and new PG synthesis at the cell center during cell division [9]. Moreover, the elongasome and the divisome interact to prepare for cell division [10], and they both consist of scaffolding cytoskeletal-like proteins, inner membrane-spanning elements, and periplasmic enzymes, including PG synthases and hydrolases [9, 11, 12]. This machinery works in concert to create the sacculus, a meshwork consisting of chains of two alternating sugar types, *N*-acetylglucosamine and *N*-acetylmuramic acid, joined through beta-(1,4)-glycosidic bonds. The stiff glycan strands are crosslinked together via peptide chains, and in *E. coli*, they are oriented helically (near perpendicularly) relative to the cell's long axis [13, 14]. In dividing model rods, the guanosine triphosphate (GTP)-dependent polymerization of the tubulin-like FtsZ creates the Z-ring (or proto-ring) [15] at the cytoplasmic face of the membrane at the center of the cell [16-18]. Once assembled, the proto-ring organizes the localization and activity of over 10 essential divisome components [12], and recently, FtsZ GTPase activity was found to determine FtsZ dynamic treadmilling in *E. coli* and *B. subtilis* [19-21].

As for the spatiotemporal regulation of the elongasome, the membrane-associated actin-like protein MreB appears to be the major scaffold for coordinating PG precursor synthesis and polymerization [22-24]. Inactivation of the *mre*B gene in *E. coli* [25, 26] and *B. subtilis* results in a change in the cell shape from rod to round [27]. MreB interacts with the inner membrane proteins MreC, MreD, and RodZ [28-32], as well as lipid II synthesis enzymes MraY and MurG [33], and its interactions and movement during elongation depends on both the synthesis of essential PG components and the activity of PG synthases [34-37]. Curiously, the intracellular pathogen *Chlamydia*—which lacks FtsZ—grows by placing new cell wall mostly at the septum using an MreB-dependent system [34].

However, alternative cell growth models do not invoke MreB polymers and hypothesize that local coordination of cell-wall-synthetizing enzymes in individual complexes is sufficient to maintain rod shape [35]. Moreover, ovococcoid bacteria that do not possess MreB homologs elongate slightly by PG synthesis that occurs in close proximity to the septation plane. This so-called preseptal growth is solely coordinated by FtsZ [36, 38, 39]. Even the model coccus *Staphylococcus aureus* grows by placing new cell wall mostly at the septum using an FtsZ-dependent system [40]. Finally, most polarly growing species, including actinobacteria and many alphaproteobacteria, do not require MreB to maintain their rod shape [41].

Based on their phylogenetic placement and shape, we hypothesized that the nematode symbionts would grow like model rods, that is predivisionally (by disperse growth) and then septally. However, ultrastructural and morphometric analyses [3, 4] indicated that widening starts at the poles of septating symbionts and proceeds toward midcell. To determine which cell wall growth mode would reconcile these observations with our predictions, we tracked the growth of *Ca*. Thiosymbion oneisti and T. hypermnestrae with a PG metabolic probe and analyzed their MreB and FtsZ localization patterns. We discovered that longitudinally dividing bacteria grow while dividing by septal, pole-to-midcell insertion of PG. Further, we showed that the actin homolog MreB is essential for both growth and division.

RESULTS

In Longitudinally Dividing Bacteria, New PG Insertion Starts at the Poles and Proceeds Centripetally

To determine the growth mode of longitudinally dividing bacteria, we incubated *Ca*. T. oneisti and T. hypermnestrae, still attached to their respective live nematode hosts, with a clickable bioorthogonal D-amino acid dipeptide ethynyl-D-alanyl-D-alanine (EDA-DA) [34, 42]. Subsequently, symbiont cells were fixed and EDA-DA was clicked (i.e., conjugated to a fluorophore) and imaged by epifluorescence microscopy or three-dimensional structured illumination microscopy (3D SIM) (Figure 1). Among the tested incubation times, 30 min and 45 min were the shortest ones resulting in detectable incorporation of new PG incorporation in *Ca*. T. oneisti (Figures S1A-S1F and S2C) and T. hypermnestrae (Figures S1G-S1L). We will henceforth refer to these incubation times as short. In *Ca*. T. oneisti, the earliest EDA-DA signal (cyan in Figures 1A and1B) appeared at both poles, albeit often with different intensities (Figure 1A, leftmost panel). In the asynchronously dividing rod *Ca*. T. hypermnestrae [4], new PG first appeared at the proximal and—only subsequently—at the distal pole (cyan in Figures 1E and1F; note the lack of distal signal in Figure 1E, leftmost and middle panels). At later septation stages, EDA-DA signal appeared closer to the cell center in both symbionts (dashed white line in Figures 1B and1F). Longer incubation times (90 min or above) resulted in a similar EDA-DA incorporation pattern, except that the septal signal was partly masked by the weak, diffuse signal likely resulting from incubating the cells for more than one generation (see representative *Ca*. T. oneisti and T. hypermnestrae cells in Figures 1C and 1D and 1G and 1H, respectively).

To gain a better resolution of the PG insertion pattern, we performed 3D SIM of *Ca*. T. oneisti and T. hypermnestrae cells subjected to long EDA-DA incubations (Figures 1D and 1H). In the case of *Ca*. T. oneisti, we detected polar arcs of newly inserted PG (Figure 1D, left panel). After septation onset, weak EDA-DA signal spanned the strong polar arcs of EDA-DA signal (Figure 1D, middle panel), and in the last septation stage, an EDA-DA ring of homogeneous signal strength appeared (Figure 1D, right panel). In the case of the *Ca*. T. hypermnestrae, we detected a strong proximal arc of EDA-DA incorporation at the septation onset (Figure 1H, left panel). At later septation stages, a distal EDA-DA incorporation arc and faint medial signal spanning the two polar arcs became visible (Figure 1H, middle panel). Finally, at the terminal stage of septation, the ring of newly synthesized PG was almost continuous (Figure 1H, right panel).

We conclude that longitudinally dividing rod-shaped *Gammaproteobacteria* grow "medially," with "medial" referring to the plane passing through the angular points (zeniths) of the symbiont poles and, therefore, parallel to the cell long axis. Medial growth implies that in nematode symbionts membrane regions of both high and low curvature are sites of active growth. Although septation and cell widening appeared to be concomitant, that is, we could not detect the disperse growth typical of model *Gammaproteobacteria*, we cannot exclude some predivisional widening. Finally, the temporal pattern of EDA-DA incorporation (Figures S1 and S2) suggests a symbiont generation time between 90 and 180 min (under experimental conditions).

FtsZ Colocalizes with Septal Insertion of New PG

The mature divisome provides the biochemical and mechanical activities required for septal PG synthesis, septation, and separation [43]. Moreover, GTPase-based FtsZ treadmilling dynamics direct the processive movement of the septal cell wall synthesis machinery in *E. coli*, thereby ensuring uniform septal cell wall synthesis and correct polar morphology, without limiting septal synthesis rate [20]. To determine whether FtsZ may place and mediate new PG insertion at the septum of longitudinally dividing bacteria, we immunostained symbionts subjected to long pulses of EDA-DA with anti-FtsZ antibody (Figures 2 and S3; Movie S1). In both *Ca*. T. oneisti and T. hypermnestrae, FtsZ localized with septal sites of PG incorporation at early (Figures 2A and 2C) and later stages of septation (Figures 2B and 2D). In *Ca*. T. hypermnestrae cells displaying an indentation of the proximal membrane (early septation stage), we detected only one proximal arc of EDA-DA incorporation (Figure 2C, upper panel) and one proximal FtsZ arc (Figure 2C,middle panel). However, at later septation stages, a distal arc of EDA-DA (Figure 2D, upper panel) and a distal arc of FtsZ (Figure 2C, middle panel) appeared. Of note, the EDA-DA and FtsZ signals were almost completely overlapping. We conclude that FtsZ localization pattern is consistent with this tubulin homolog placing and mediating septal PG insertion in longitudinally dividing rods.

MreB Polymers Localize Medially throughout the Cell Cycle

MreB localizes in the cylindrical part of *E. coli* [32, 44, 45], and it has been shown to form discrete, motile patches that move, independently of MreB polymerization or treadmilling, near perpendicularly to the long cell axis in *E. coli*, *B. subtilis*, and *C. crescentus* [39, 46-48]. Moreover, *in vivo* labeling and immunostaining of *E. coli* MreB resulted in the detection of ring-like structures at the center of dividing cells in addition to the punctate pattern present along the cell periphery [10, 49]. To assess the role of MreB in the growth of nematode symbionts, we immunostained *Ca*. T. oneisti and T. hypermnestrae cells with an anti-MreB antibody (Figure S3), and its localization pattern is displayed in Figures 3 and 4. Epifluorescence microscopy indicates that MreB polymers run medially (Figures 3A and 3C, respectively; longitudinal orientation of MreB polymers was confirmed by 3D SIM; Figure 4). Moreover, we plotted the total MreB fluorescence of non-constricted and constricted cells against the normalized cell width (Figures 3B and 3D for *Ca*. T. oneisti and T. hypermnestrae, respectively). MreB accumulates in the central part of the short axis of constricted *Ca*. T. oneisti and T. hypermnestrae (Figures 3B and 3C, respectively). Of note, at late septation stages (Figure S4), distal accumulation of *Ca*. T. hypermnestrae MreB

mirrored distal PG insertion (Figures 1F and S4E) and distal FtsZ accumulation (Figure 2 and as shown in [4]).

In order to confirm that MreB polymers are aligned parallel to the long axis and to gain a better resolution of their localization, we subjected immunostained *Ca*. T. oneisti (Figures 4A-4E) and T. hypermnestrae to 3D SIM analysis (Figures 4F-4J; Movies S2 and S3). In non-constricted *Ca*. T. oneisti and T. hypermnestrae cells, MreB is medial, and a discontinuous ring running from pole to pole is clearly recognizable in the latter (Figures 4A and 4B for *Ca*. T. oneisti and Figure 4F for *Ca*. T. hypermnestrae). However—as the septum forms and closes—MreB is progressively excluded from the septum and localizes medially in each of the two prospective daughter cells (Figures 4C-4E for *Ca*. T. oneisti and Figures 4G-4J for *Ca*. T. hypermnestrae). Despite being medial (Figures 3 and 4), MreB barely overlaps with septal EDA-DA (Figure S5), suggesting that FtsZ, rather than MreB, mediates the building of the septum.

In conclusion, we showed that MreB accumulates medially throughout the cell cycle in longitudinally dividing bacteria and it is not excluded from membrane regions of high curvature as observed in *E. coli* and *B. subtilis*.

MreB Accumulates Medially Prior to FtsZ

In *E. coli*, MreB midcell rings colocalized with and were never observed independently of FtsZ proto-rings [10, 49]. To analyze MreB localization with respect to FtsZ, we immunostained *Ca*. T. oneisti with anti-FtsZ and -MreB antibodies (Figure 5). Comparison of FtsZ (Figure 5B) and MreB (Figure 5A) demographs, and of total FtsZ and total MreB fluorescence plotted against normalized cell width (Figures 5C and 5D), as well as images of representative cells (Figures 5E-5H), indicated that MreB is medially localized prior to FtsZ. Colocalization of MreB and FtsZ fluorescence signals was quantified by using the Pearson's coefficient, and we observed a considerable overlap between the two fluorescence signals in all cells (average Pearson's coefficient of 0.45 on a scale of −1.0 to 1.0; Figure S6).

We conclude that—in contrast to what was reported for *E. coli*—in *Ca*. T. oneisti and T. hypermnestrae, MreB is localized at the prospective septation plane prior to divisome assembly. Therefore, based on its localization pattern, MreB may mediate FtsZ proto-ring assembly in longitudinally dividing bacteria.

MreB Depolymerization Blocks Insertion of Newly Synthesized PG

Localization pattern analysis of newly inserted PG, FtsZ, and MreB suggested that FtsZ mediates septum synthesis (Figures 2 and 5) and that MreB mediates preseptal widening and divisome assembly (Figures 3, 4, and 5). Given that direct interaction of FtsZ and MreB supports septum synthesis and cell division in *E. coli* [49], we applied the MreB polymerization inhibitor S-3,4-dichlorobenzyl-isothiourea (A22) to the symbionts to understand the role of MreB polymers in *Ca*. T. oneisti and T. hypermnestrae division. Importantly, A22 is not toxic to *Chromadorea* nematodes at the used concentration and incubation times (Table S1). Further, the amino acids that make up the ATP-binding pocket to which A22 is predicted to bind, as well as the amino acids that—if mutated—confer A22 resistance are conserved between *E. coli, Ca*. T. oneisti, and *Ca*. T. hypermnestrae [50]

(Figure S7). As expected from the symbiont MreB protein primary structures, A22 incubation affected medial MreB polymerization in both non-constricted and constricted symbionts (Figures 6A, 6B, and 6E for *Ca*. T. oneisti and Figures 6C-6E for T. hypermnestrae). Surprisingly, insertion of newly synthesized PG in *Ca*. T. oneisti and T. hypermnestrae was not only reduced but abolished (Figure 6E). Moreover, we observed a decrease of total medial FtsZ fluorescence (Figures 6F and 6G for *Ca*. T. oneisti and Figures 6I-6K for T. hypermnestrae), and FtsZ ring-like structures were barely recognizable in non-constricted and constricted *Ca*. T. oneisti (Figure 6H) and not at all in *Ca*. T. hypermnestrae (Figure 6L). Consistently, the average number of constricted cells decreased significantly ($p = 0.001$ for *Ca*. T. oneisti and $p = 0.003$ for *Ca*. T. hypermnestrae; Figures 6M and 6N, respec-tively; Table S4).

We conclude that the bacterial actin homolog is required for cell growth and division in longitudinally dividing *Gammaproteobacteria*.

DISCUSSION

We investigated the growth mode of two longitudinally dividing symbionts to know whether (1) it may be polarized toward the host attachment site and whether (2) transversal arrangement and polar exclusion of MreB polymers are essential for rod shape maintenance. We found that *Ca*. T. hypermnestrae orients its cell growth synthesis machinery toward the host attachment site. Indeed, in this symbiont, new PG insertion starts at the proximal, nematode-attached pole by default. Strikingly, at the molecular level, the novelty of symbiont cell growth is three-fold: (1) these *Gammaproteobacteria* start to grow at PG regions traditionally thought to be inert in model rods; (2) cell wall growth is mainly (if not only) septal as observed in model ovococci and cocci, but—differently from these—it is MreB-mediated; and (3) MreB appears to localize medially prior to divisome assembly and is required for septal growth.

Beside the nematode symbionts, the actinobacterium *Streptomices coelicolor* and the *Alphaproteobacteria Agrobacterium tumefaciensis*, and *Brucella suis* [51] also have growing poles. However, *Ca*. T. hypermnestrae is unique in that PG insertion initiates at the host-attached pole and is accompanied by asymmetric, FtsZ-mediated membrane invagination [4]. Although asymmetric cell growth has been observed in a variety of gram-negative bacteria, including *Proteus mirabilis* and *Caulobacter crescentus* [51], *Ca*. T. hypermnestrae is the first to show animal host polarization of the PG synthesis machinery. The septal EDA-DA incorporation observed in dividing symbionts is similar to that reported for model cocci [52] and suggests that cell widening occurs during septation. Whereas we could not observe predivisional, disperse growth in the nematode symbionts, in *E. coli* and *B. subtilis*, disperse growth of the lateral walls is detectable even upon short fluorescent D-amino acids pulses [42].

Recent work indicates that, in *E. coli*, MreB preferentially localizes to and directs PG synthesis laterally (i.e., at regions of low curvature) and not at the poles [32, 44, 45, 53]. This can be explained by the fact that the poles are enriched in anionic phospholipids (phosphatidylglycerol and cardiolipin), which preferentially interact with monomeric MreB

in vitro [45, 54]. Therefore, it has been hypothesized that exclusion of MreB polymers at the poles is necessary to enable cells to elongate bidirectionally only in their cylindrical part [45]. Although the lipid composition of the symbionts' membranes is still under investigation, symbiont MreB localizes in areas of both low and high curvature (i.e., not only in the cylindrical part but also at the poles). The presence of MreB throughout the cell long axis in both *Ca*. T. oneisti and T. hypermnestrae would enable them to branch and double their poles. However, differently to what was observed in *E. coli* cells that artificially express MreB at their poles [45], symbiont cells maintain their rod shape and polarity despite polar bifurcation. One possible explanation could be that—in the symbionts—polar bifurcation is mediated by medial PG insertion and this, in turn, is coupled to FtsZ-based longitudinal division.

When *E. coli* is treated with the MreB-depolymerizing drug A22, MreB localization becomes diffuse and ubiquitous, and the cells become round after at least two generations [25, 26, 55, 56]. Moreover, the orientation of MreB polymers relative to the *E. coli* long axis correlates with cell diameter, which led to propose that MreB polymers are responsible for the diameter of the cell wall [50]. On the other hand, *mre*B mutants capable to accommodate to different cell widths suggested that MreB might function as a width-maintaining rather than a width-determining factor [37, 57]. In *Ca*. T. oneisti and T. hypermnestrae, A22 altered both MreB and FtsZ localization patterns (Figure 6), but the nematode symbionts did not become round (Table S2). Instead, in line with PG incorporation abolishment, A22 treatment resulted in a decrease in the number of constricted *Ca*. T. oneisti and T. hypermnestrae cells (Figures 6M and 6N, respectively). Thus, the presence of medial, functional MreB and its direct interaction with FtsZ may be required for symbiont division. As the symbiont MreB amino acid required for FtsZ interaction is conserved [49] (Figure S7), loss of MreB-FtsZ interaction could directly affect FtsZ proto-ring formation. The septation defects observed upon MreB depolymerization are in line with what was reported for pathogenic *Chlamydia*. In these obligate intracellular pathogens that lack FtsZ, inhibition of MreB polymerization blocks PG synthesis and affects replication [34]. As for *E. coli*, *mre*B gene loss of function also affects the division rate. However, this only seems to be an indirect effect of the A22-induced spherical shape, which requires the construction of a bigger septum [10]. Indeed, division rate is not affected in *mre*B deletion mutants in which PBP3, PBP1B, and FtsZ are overproduced [25, 58]. What the symbionts, pathogenic *Chlamydia* and *E. coli* have in common is that—despite the A22-induced mislocalization of MreB—misplacement of their septation planes was never observed.

A22 can have an MreB-independent toxic effect on bacterial growth [59]. This toxicity is consistent with the finding that, given that it binds to MreB as a low-affinity ADP imitator, A22 may affect other nucleotide-binding processes [60]. In this study, we employed A22 at 20 μg/mL based on a previous work showing that this concentration depolymerized MreB filaments but affected neither the growth rate of *E. coli* nor its DNA replication or segregation [55]. The amino acids that make up the ATP-binding pocket to which A22 is predicted to bind, as well as the amino acids that—if mutated—confer A22 resistance, are conserved between *E. coli*, *Ca*. T. oneisti, and *Ca*. T. hypermnestrae (Figure S7). Therefore, it is safe to assume that the affinity of A22 for MreB is similar among these three *Gammaproteobacteria*. However, to confirm that the A22-induced septation defects observed

in the symbionts are not due to off-target toxicity, additional inhibitor studies employing less toxic A22 an-alogs, such as MP265, should be performed.

The fact that MreB is medial throughout the life of the symbionts suggests that, differently to what was observed previously [49], medial FtsZ polymers are not necessary to recruit MreB to the septation plane. Considering the FtsZ localization and septation defects observed in A22-treated symbionts, the opposite scenario seems likelier (i.e., MreB-mediated FtsZ localization).

The conservation of protein classes for PG synthesis machinery across gram-negative and positive bacteria, and between the elongasome and divisome, suggests a general strategy for shaping the bacterial cell, as well as a common evolutionary history [61]. However, if penicillin-binding proteins (PBPs) catalyze PG growth and maturation throughout the bacterial kingdom, different PBPs have different functions. The *E. coli* class A (bi-functional) PBPs PBP1A, PBP1B, and PBP1C have glycosyltransferase and transpeptidase activities. The class B PBPs are monofunctional transpeptidases that crosslink PG subunits [62]. Two of these, PBP2 and PBP3, are present in *E. coli* and have different cellular functions [63]: inactivation of PBP2 inhibits cell elongation and results in spherical shape, whereas inactivation of PBP3 blocks new cell pole synthesis (septation) and results in filamentation. However, PBP2 also localizes transiently at midcell, thereby overlapping and interacting with PBP3 during the onset of the divisome [10, 64]. It was therefore proposed that the transient positioning of the elongasome and divisome at midcell in a preparative division phase mediates preseptal PG synthesis. In our symbionts, following short incubations with EDA-DA, the first detectable PG insertion was at the leading edges of the constricting cell envelope. This could be due to the fact that, in *E. coli*, completely new PG is synthesized for septal growth, whereas dispersed insertion of already available lipid II elongates its cylindrical part [7]. If this holds true for the symbionts, septal EDA-DA incorporation would be favored over preseptal incorporation and, as a consequence, if this is not as extensive as in *E. coli*, would not be detectable by using EDA-DA. Nevertheless, (1) polar incorporation in non-constricted symbionts (Figures 1A and 1E) and (2) the bone-like and pear-like shape of *Ca*. T. oneisti and T. hypermnestrae cells that have just started septation, respectively, suggest that MreB might mediate PG incorporation at the poles shortly before divisome maturation. In analogy with *E. coli*, PBP1A/PBP2 might synthesize new cell wall prior to PBP3 at the septation plane [10]. Although the available genome drafts indicate the presence of PBP1A, PBP2, and PBP3/FtsI, as well as RodA, RodZ, and the MraY and Mur enzymes for lipid II synthesis, their localization patterns await to be described.

Intriguingly, MreB exclusion from the divisome in concomitance with furrow ingression is in line with published models where the absence of MreB polymers is a prerequisite for septation [10, 65-67]. As the divisome matures and a PG-synthetizing enzyme (possibly a PBP3 ortholog) accumulates medially, the elongasome would be more and more excluded until it cannot participate in septal PG synthesis (in case it ever did).

Our data suggest that MreB mediates and places divisome assembly, but what drives centripetal new PG insertion at the septum? It has been recently discovered that *B. subtilis*

FtsZ treadmills circumferentially around the division ring and drives the motions of the PG-synthesizing enzymes. The FtsZ treadmilling rate controlled both the rate of PG synthesis and cell division [21]. Similarly, GTPase-activity-coupled FtsZ treadmilling guides the progressive insertion of new cell wall by building increasingly smaller concentric rings of PG to divide the cell in *E. coli* [20]. Given that FtsZ signal overlapped with new PG insertion (in particular at the leading edges of membrane constriction), we hypothesize that FtsZ, possibly together with FtsA, organizes septal cell wall in the symbionts. In the absence of available genetic tools, *in vitro* reconstitution of cell wall synthesis will hopefully shed light on how the FtsZ-mediated processes of septation and membrane ingression are coupled.

To sum up, we propose that longitudinally dividing rods grow as follows (Figure 7): in new-born cells, MreB is localized medially and, before FtsZ polymerizes into a ring-like structure, new PG is inserted at the poles (both poles in the case of *Ca*. T. oneisti and at the proximal pole only in the case of *Ca*. T. hypermnestrae). Notably, functional MreB is required for medial FtsZ proto-ring formation in the symbionts. As septation proceeds, FtsZ organizes progressive and centripetal PG insertion at the septum. Given the limited width of the symbionts, septal growth alone could be sufficient for cell widening. However, we cannot exclude the existence of some MreB-mediated preseptal growth. As septation approaches completion, MreB is more and more excluded from the constricting membrane but already medially localized in each of the two prospective daughter cells.

If it is clear that the geometric cues that have been proposed to guide MreB localization in *E. coli* or *B. subtilis* are reversed in the symbionts, one may argue that the symbionts' growth mode has not evolved by reorienting the cytokinetic and PG synthesizing machineries of 90 degrees to position the septation plane parallel to the cell long axis. Instead, the symbionts represent standard *Gammaproteobacteria* with an extremely short long axis and a considerably increased cell width. In this valid, evolutionary sound scenario, the symbiont cell poles would be functionally equivalent to the *E. coli* lateral sides (and vice versa) and the medial position of symbiont would correspond to the midcell position of *E. coli*. Because, in this scenario, the symbionts would consist almost exclusively of virtually inert poles, MreB would have the same circumferential orientation as in *E. coli* but only have a thin (medial) band to localize within, distant from the inert sides of the cell. If we consider the symbionts as merely "squeezed" *E. coli* cells, the cytokinetic (FtsZ-based) machinery and the cell growth machinery would mesh to a point where—due to the extremely low amount of "active" membrane regions—it would be hard to observe predivisional widening and/or septal FtsZ prior to septal MreB. However, if *Ca*. T. oneisti may be regarded as a "squeezed" *E. coli*, this cannot be the case for *Ca*. T. hypermnestrae, which shows a strong polarization of both cytokinetic and growth machineries. The latter point implies that *Ca*. T. hypermnestrae has three functionally different membrane regions instead of the canonical two: the lateral side, the free pole, and the nematode-attached pole previously shown to be fimbriae-rich [4]. Future research will hopefully clarify how reversed geometric cues are integrated with host-attachment cues to guide symbiont MreB and FtsZ localization.

MreB-mediated septal growth has only been observed in animal-associated rods. However, given that we do not know how the free-living counterparts of the symbionts—if existing—

reproduce, it is unclear whether host-polarized cell growth is an adaptation to the symbiotic lifestyle. Longitudinal fission and concomitant septal growth might have evolved to guarantee host attachment to both daughter cells while maximizing symbiont cell number. To grasp the functional significance of hostpolarized cell growth, we need to better understand symbionts' physiology. Nevertheless, our work suggests that environmental cues can induce an inversion of the cellular dimensions so that even fundamental biological processes can be reoriented without the need to substitute the underlying molecular key players.

STAR★METHODS

CONTACT FOR REAGENT AND RESOURCE SHARING

Further information and requests for resources and reagents should be directed to and will be fulfilled by the Lead Contact, Silvia Bulgheresi (silvia.bulgheresi@univie.ac.at).

EXPERIMENTAL MODEL AND SUBJECT DETAILS

Both *Ca*. T. oneisti and T. hypermnestrae are not cultivable and can only be accessed by collecting their marine nematode hosts, *L. oneistus* and *R. hypermnestrae*, respectively. The latter were collected on multiple field trips (2014-2016) in approximately ~1 m depth from a sand bar off Carrie Bow Cay, Belize (16°48'11.01"N, 88°4'54.42"W). Specimens of *L. oneistus* and *R. hypermnestra* were extracted from the sand by stirring it in seawater and pouring the supernatant through a 63 μm mesh sieve. The retained material was transferred into a Petri dish and single nematodes were handpicked using pipettes under a dissecting microscope. Symbiotic nematodes were transported from Carrie Bow Cay to the University of Vienna deep-frozen.

METHOD DETAILS

A22 toxicity tests on Caenorhabditis *elegans*

Wild-type *C. elegans* was grown on nematode growth medium (NGM) plates seeded with *E. coli* OP50 [69]. L4 stage populations were synchronized with alkaline bleach solution [69] and washed with autoclaved M9 buffer (0.3% KH2PO4, 0.6% Na2HPO4, 0.5% NaCl, 1 mM MgSO4) prior exposure to 20 μg/ml A22 in M9 buffer at 20°C or to M9 without A22 (negative control) for 2, 4, 8, 24, 48, 72 h. Toxicity test was performed in duplicates (i.e., two worm batches were exposed to M9 with A22 and two were exposed to M9 without A22). After treatment, to evaluate A22 toxicity, nematodes were washed three times with M9 and put on NGM plate with 25 μM 5-fluoro-2′-deoxyuridine (FuDR) [70] to prevent synchronous C. *elegans* populations from reproducing. See also Table S1.

EDA-DA and A22 incubation of live symbionts

To track symbiont cell wall growth, batches of approx. 50 live symbiotic nematodes were each incubated in a 1.5 mL tube containing 500 μl of 10 mM ethynyl-D-alanyl-D-alanine (EDA-DA, a D-amino acid carrying a clickable ethynyl group) in filter sterilized natural seawater (FSW) for 5 to 480 min. For each A22 treatment, batches of approx. 40 live

symbiotic nematodes were incubated in 1.5 mL tubes containing 500 µl of 20 µg/ml A22 (Sigma-Aldrich) in FSW for 2 h prior addition of EDA-DA and an additional 90 min-long incubation (A22 was not removed upon addition of EDA-DA). Given that A22 was dissolved in DMSO so that a 1:10,000 dilution of this compound was finally present in the incubation medium, DMSO was added in the same amount (1:10,000 dilution) to negative control nematodes, that is to nematodes not treated with A22. The total duration of the A22 treatment was 210 min or 8 hr. Upon incubation in either EDA-DA only or in EDA-DA and A22, nematodes were washed once in FSW, transferred to methanol, and stored at −20°C. Nematodes were transported from Carrie Bow Cay to the University of Vienna deep-frozen.

Cloning of symbiont *mreB* genes

We used the genome drafts of *Ca*. T. oneisti [71] and *Ca*. T. hypermnestrae (available under request at http://rast.nmpdr.org/rast.cgi) to design specific primers against *Ca*. T. hypermnestrae and *Ca*. T. oneisti *mre*B genes, respectively. Methanol fixed deep-frozen worms were rehydrated in phosphate-buffered saline (PBS) and bacteria were detached by sonication. Subsequently, 2 µl of bacterial suspension were used as template in each 50 µl PCR reaction. A 1,047 nucleotide (nt)-long and a 1,059 nt-long *mreB* gene fragment were amplified from *Ca*. T. oneisti and T. hypermnestrae, respectively, using the forward primer LosRhsMreB_F (5′- ATGTTTCTCCGACGCATTCGAG-3′) and the reverse primers LosMreB_R (5′-CTACTCCGTCATAGCCAACAGGTC-3′) or RhsMreB_R (5′-TTACTCGACCACGGTGAACAAATC-3′). PCR conditions were as follows: 95°C for 5 min, followed by 30 cycles at 95°C for 45 s, 60°C for 45 s, 72°C for 75 s, followed by a final elongation step at 72°C for 10 min. We randomly picked and fully sequenced four clones containing the *Ca*. T. hypermnestrae gene fragment and four clones containing the *Ca*. T. oneisti *mre*B gene fragment in both directions. Sequences were aligned and compared with CodonCode Aligner 3.7.1 software (CodonCode Corporation, Dedham, MA, USA). A predicted 348 aa-long MreB protein (ToMreB) is encoded by a 1,047 nt-long ORF in *Ca*. T. oneisti (GenBank accession number MF350658) and a 352 aa-long MreB protein (ThMreB) is encoded by a 1,059 nt-long ORF (GenBank accession number MF317948) in *Ca*. T. hypermnestrae.

Cloning, expression and purification of MreB from *Ca*. T. oneisti

The *mreB* gene of *Ca*. T. oneisti was cloned into pTB146 vector [72] by Gibson assembly and a His-tagged MreB recombinant protein (H-S-MreB) was expressed in *E. coli* strain BL21(DE3) pLysS. Primers used to obtain the fragments for Gibson assembly were pML118-his-sumo-losMreB-fw (5′-TCACAGAGAACAGATTGGTGGGATGTTTCTCCGACGCATTCG-3′) and pML118-hissumo-losMreB-rev (5′-CTTCCTGCAGTCACCCGGGCCTCCGTCATAGCCAACAGGT-3′) for the *mreB* gene of *Ca*. T. oneisti and pML118-vector-his-sumo-fw (5′-GCCCGGGTGACTGCAGGAAG-3′) and pML118-vector-his-sumo-rev (5′- CCCACCAATC TGTTCTCTGTGA-3′) for the vector backbone. PCR conditions were as follows: 98°C for 10 min, followed by 35 cycles at 98°C for 30 s, 58°C for 30 s, 72°C for 90 s (*mreB* gene) or 5 min (vector), followed by a final elongation step at 72°C for 10 min. The H-S-*mreB* recombinant strain was grown in Tryptone Yeast (TY) medium with 100 µg/ml ampicillin and 25 mg/ml chloramphenicol at

37°C. The recombinant protein was induced by adding 0.5 mM IPTG. After 3 h induction, the culture was pelleted at 8,000 rpm and resuspended in 8M urea phosphate buffer (pH = 8). Cells were passed through a French press and cell lysates separated into pellet and supernatant fractions by ultracentrifuge 210,000 rpm 45 min. The purification was performed by ÄKTA FPLC (GE Healthcare). The supernatant was applied to HiTrap TALON® crude (GE Healthcare) 1 mL column, and the column was washed by phosphate buffer (pH = 8) with 8M urea and 10 mM imidazole followed by elution of His-S-MreB by phosphate buffer (pH = 8) supplemented with 8 M urea and 200 mM Imidazole.

Immunoaffinity purification of a polyclonal anti-*E. coli* MreB antibody

Purified H-S-MreB (50 μg) was applied to a 2-cm nitrocellulose membrane (Bio-Rad). Membrane was blocked for 1 h in 5% non-fat milk in Tris-buffered saline (TBS; pH = 7.4) at room temperature and subsequently incubated with 20 μl of polyclonal anti-*E. coli* MreB antibody (1:50 dilution in TBS) at 4°C overnight. The membrane was washed three times with TBS and subsequently the antibody was eluted with 100 μL 0.1 M glycine-HCl pH = 2.7. The eluted antibody was neutralized immediately by 8.7 μL 1 M Tris-HCl pH = 8.5. The activity of the immunoaffinity purified antibody was verified by immunostaining *E. coli* cells.

Western Blots

Methanol fixed deep-frozen worms were rehydrated in PBS and, subsequently, proteins from dissociated symbionts were separated by reduced sodium dodecyl sulfate (SDS)-polyacrylamide gel electrophoresis (PAGE) on NuPAGE 4%–12% Bis-Tris pre-cast gels (Invitrogen), followed by transfer to Hybond ECL nitrocellulose membranes (Amersham Biosciences). Membranes were blocked 45 min in phosphate-buffered saline (PBS) containing 5% (wt/vol) nonfat milk (PBSM) at room temperature and incubated overnight at 4°C with a 1:10 dilution of rabbit polyclonal anti-*E. coli* MreB antibody [10] purified against H-S-MreB and with a rabbit polyclonal anti-*Ca*. T. oneisti FtsZ peptide antibody (1:500; Genosphere Biotech) in PBSM. For the negative control, the primary antibody was omitted at this step. After three washing steps in PBSM, the blots were incubated for 1 h at room temperature with a horseradish peroxidase-conjugated anti-rabbit secondary antibody (1: 5,000; Amersham Biosciences) in PBSM. Protein-antibody complexes were visualized using ECL Plus detection reagents and films (Amersham Biosciences).

Immunostaining

Deep-frozen methanol fixed nematodes were rehydrated and washed in PBS containing 0.1% Tween 20 (PBT), followed by permeabilization of the bacterial PG by incubation for 10 min with 0.1% (wt/vol) lysozyme at room temperature. Blocking was carried out for 1 h in PBT containing 2% (wt/vol) bovine serum albumin (blocking solution) at room temperature. *Ca*. T. oneisti and T. hypermnestrae were incubated with a 1:1 dilution of immunoaffinity purified rabbit polyclonal anti-*E. coli* MreB antibody (see previous section), as well as with a 1:500 dilution of rabbit polyclonal anti-*Ca*. T. oneisti FtsZ peptide antibody (Genosphere Biotech) in the case of *Ca*. T. oneisti, or with a 1:200 dilution of rabbit polyclonal anti-*E. coli* FtsZ antibody [4, 73] in the case of *Ca*. T. hypermnestrae. All primary antibodies were incubated overnight at 4°C in blocking solution. Upon incubation with

primary antibody (or without in the case of the negative control) samples were washed three times in PBT and incubated with a 1:500 dilution of secondary Alexa555-conjugated anti-rabbit antibody (Jackson ImmunoResearch, USA) in blocking solution for 1 h at room temperature. Unbound secondary antibody was removed by three washing steps in PBT and worms were sonicated for 40 s to dissociate *Ca*. T. oneisti and T. hypermnestrae cells from their hosts prior mounting. 1 μl of the bacterial solution was mixed with 0.5 μl of Vectashield mounting medium (Vector Labs).

Click-chemistry

Deep frozen methanol fixed nematodes were rehydrated and washed in PBS containing 0.1% Tween 20 (PBT). Blocking was carried out for 30 min in PBT containing 2% (wt/vol) bovine serum albumin (blocking solution) at room temperature. An Alexa488 fluorophore was covalently bound to EDA-DA via copper catalyzed click-chemistry by following the user manual protocol for the Click-iT reaction cocktail (Click-iT EdU Imaging Kit, Invitrogen). The nematodes were incubated with the Click-iT reaction cocktail for 30 min at RT in the dark. Unbound dye was removed by a 10-min wash in PBT and one wash in PBS. Worms were sonicated for 40 s to dissociate *Ca*. T. oneisti and T. hypermnestrae prior mounting. For immunostaining of clicked bacterial cells, worms were washed for 10 min in PBT and subsequently incubated with blocking solution for 30 min at room temperature in the dark. From here on, immunostaining was performed as described above, except that PG permeabilization was omitted and all steps were carried out in the dark to prevent bleaching of clicked cells.

Morphometric and fluorescence measurements

Symbiont cells were dissociated from fixed untreated and A22-treated *L. oneistus* nematodes, and from untreated and A22-treated *R. hypermnestrae* nematodes by sonication. Cell suspensions were applied to an 1% agarose covered microscopy slide [68] and imaged using a Nikon Eclipse 50i microscope equipped with either DS-Qi1mc camera, an Orca Flash 4.0 (Hamamatsu, Japan) or a MFCool camera (Jenoptik, Germany). Epifluorescence images were acquired using the NIS-Elements AR 4.20.01 software (Nikon) or the ProgRes Capture Pro 2.8.8 software (Jenoptik) and processed using the public domain program ImageJ [74] in combination with plugin ObjectJ and a modified version of Coli-Inspector [10, 73]. Cell outlines were traced and cell length, width and fluorescence patterns were measured automatically. Automatic cell recognition was double-checked manually. For the average fluorescence plots and for the demographs, cells were automatically grouped into morphological classes based on phase-contrast images, each cell was resampled to the same length and the fluorescence intensities added up and averaged. For assessing the effects of A22, symbiont cells were grouped into constricted and non-constricted based on visual inspection. Data analysis was performed using Excel 2016 (Microsoft Corporation, USA), plots were created with Excel 2016 and figures were compiled using Photoshop CS6 and Illustrator CS 6 (Adobe Systems Inc. USA).

Three-Dimensional Structured Illumination Microscopy (3D SIM) imaging and analysis

Cell suspensions were applied on high precision coverslips (No. 1.5H, Sigma-Aldrich) coated with 0.01% (wt/vol) of Poly-L-Lysin. After letting the cell dry onto the surface of the

coverslip, antifade mounting medium (Vectashield) was applied and the coverslip was sealed to a slide. 3D SIM was performed on a Delta Vision OMX v4 microscope equipped with an Olympus 60X/1.42 Oil Plan Apo N objective and 2 sCMOS cameras. The samples were excited with lasers at 488 nm and at 568 nm, the emission was detected through emission filters 477/32 nm and 571.5/19 nm (Center/Bandpass), respectively. The image reconstruction and registration was performed using the SoftWoRx image software running under Linux operating system. Differential interference contrast (DIC) images were used to select representative cells and to create cell outlines. For further image analysis of SIM image z stacks we used Fiji (ImageJ) Version 2.0.0-rc-54/1.51h. Namely, we assigned a color to each channel (Lookup Tables, cyan and red hot), stacks were fused to a single image (z projection, maximum intensity), stacks were rotated 90° (resliced) prior z projection for the side view, and videos were created via 3D projection. Regions of interest were cut out and, for uniformity, placed on a black squared background. Figures were compiled using Photoshop CS6 and Illustrator CS 6 (Adobe Systems Inc. USA).

QUANTIFICATION AND STATISTICAL ANALYSIS

Statistical analysis of number of constricted cells

For assessing the effects of A22 on septation, symbiont cells dissociated from 10 untreated and 10 A22-treated *L. oneistus* nematodes, and from five untreated and five A22-treated *R. hypermnestrae* nematodes were grouped into constricted and non-constricted based on visual inspection (Table S3). We analyzed whether the number of constricted cells for untreated and A22-treated *Ca*. T. oneisti and T. hypermnestrae were normally distributed by performing two tests of normality (Kolmogrov-Smirnov and Shapiro-Wilk; Table S4). An unpaired t-Test revealed significant difference ($p < 0.05$) between untreated and A22-treated cells for both *Ca*. T. oneisti and T. hypermnestrae (Table S4; a significance level of 95% ($\alpha = 0.05$) was set for all the tests). Boxplots were created by SPSS 19.0 (SPSS, IL USA).

Supplementary Material

Refer to Web version on PubMed Central for supplementary material.

ACKNOWLEDGMENTS

This work was supported by the Austrian Science Fund (FWF) grant P22470 (N.L. and S.B.), a uni:docs fellowship and a PhD completion grant 2016 from the University of Vienna (N.P.), grant 201506760048 from the China Scholarship Council (J.W.), FWF project P28593 (P.M.W.), grants R01GM51986 and R35GM122556 from the NIH (Y.V.B.), and grant R01GM113172 from the NIH (M.S.V. and Y.V.B.). We are extremely grateful to Lijuan Zhang and Kareem Elsayad (Vienna Biocenter Core Facility for Advanced Microscopy) for technical support with 3D SIM, to Norbert Vischer for image analysis programming, and to Gabriela Paredes (Dep. Ecogenomics and Systems Biology, University of Vienna) and Veronika Plichta for statistical analysis. The wild-type *C. elegans*, NGM, FuDR, and M9 buffer in this study were provided by Belinda Koenders-van Sintanneland (Faculty of Science, University of Amsterdam), whom we thank for her help with A22 toxicity tests on nematodes. We are extremely grateful to Sven van Teeffelen, K.C. Huang, Martin Loose, and two anonymous reviewers for their very constructive comments. This work is a contribution from the Carrie Bow Cay Laboratory, Caribbean Coral Reef Ecosystem Program, National Museum of Natural History, Washington, DC.

REFERENCES

1. Polz MF, Distel DL, Zarda B, Amann R, Felbeck H, Ott JA, and Cavanaugh CM (1994). Phylogenetic analysis of a highly specific association between ectosymbiotic, sulfur-oxidizing bacteria and a marine nematode. Appl. Environ. Microbiol. 60, 4461–4467. [PubMed: 7529016]
2. Ott JA, Gruber-Vodicka HR, Leisch N, and Zimmermann J (2014). Phylogenetic confirmation of the genus *Robbea* (Nematoda: Desmodoridae, Stilbonematinae) with the description of three new species. Syst. Biodivers. 12, 434–455. [PubMed: 27630534]
3. Leisch N, Verheul J, Heindl NR, Gruber-Vodicka HR, Pende N, den Blaauwen T, and Bulgheresi S (2012). Growth in width and FtsZ ring longitudinal positioning in a gammaproteobacterial symbiont. Curr. Biol. 22, R831–R832. [PubMed: 23058799]
4. Leisch N, Pende N, Weber PM, Gruber-Vodicka HR, Verheul J, Vischer NOE, Abby SS, Geier B, den Blaauwen T, and Bulgheresi S (2016). Asynchronous division by non-ring FtsZ in the gammaproteobacterial symbiont of *Robbea hypermnestra*. Nat. Microbiol. 2, 16182. [PubMed: 27723729]
5. Mobley HL, Koch AL, Doyle RJ, and Streips UN (1984). Insertion and fate of the cell wall in *Bacillus subtilis*. J. Bacteriol. 158, 169–179. [PubMed: 6232259]
6. Schlaeppi JM, Schaefer O, and Karamata D (1985). Cell wall and DNA cosegregation in *Bacillus subtilis* studied by electron microscope autoradiography. J. Bacteriol. 164, 130–135. [PubMed: 3930463]
7. de Pedro MA, Quintela JC, Höltje JV, and Schwarz H (1997). Murein segregation in *Escherichia coli*. J. Bacteriol. 179, 2823–2834. [PubMed: 9139895]
8. Janakiraman A, and Goldberg MB (2004). Evidence for polar positional information independent of cell division and nucleoid occlusion. Proc. Natl. Acad. Sci. USA 101, 835–840. [PubMed: 14715903]
9. Typas A, Banzhaf M, Gross CA, and Vollmer W (2011). From the regulation of peptidoglycan synthesis to bacterial growth and morphology. Nat. Rev. Microbiol. 10, 123–136. [PubMed: 22203377]
10. van der Ploeg R, Verheul J, Vischer NOE, Alexeeva S, Hoogendoorn E, Postma M, Banzhaf M, Vollmer W, and den Blaauwen T (2013). Colocalization and interaction between elongasome and divisome during a preparative cell division phase in *Escherichia coli*. Mol. Microbiol. 87, 1074–1087. [PubMed: 23387922]
11. Margolin W (2009). Sculpting the bacterial cell. Curr. Biol. 19, R812–R822. [PubMed: 19906583]
12. Egan AJF, and Vollmer W (2013). The physiology of bacterial cell division. Ann. N Y Acad. Sci. 1277, 8–28. [PubMed: 23215820]
13. Deng Y, Sun M, and Shaevitz JW (2011). Direct measurement of cell wall stress stiffening and turgor pressure in live bacterial cells. Phys. Rev. Lett. 107, 158101. [PubMed: 22107320]
14. Wang S, Furchtgott L, Huang KC, and Shaevitz JW (2012). Helical insertion of peptidoglycan produces chiral ordering of the bacterial cell wall. Proc. Natl. Acad. Sci. USA 109, E595–E604. [PubMed: 22343529]
15. Rico AI, Krupka M, and Vicente M (2013). In the beginning, *Escherichia coli* assembled the proto-ring: an initial phase of division. J. Biol. Chem. 288, 20830–20836. [PubMed: 23740256]
16. Bi EF, and Lutkenhaus J (1991). FtsZ ring structure associated with division in *Escherichia coli*. Nature 354, 161–164. [PubMed: 1944597]
17. Löwe J, and Amos LA (1998). Crystal structure of the bacterial cell-division protein FtsZ. Nature 391, 203–206. [PubMed: 9428770]
18. Mukherjee A, and Lutkenhaus J (1998). Dynamic assembly of FtsZ regulated by GTP hydrolysis. EMBO J. 17, 462–469. [PubMed: 9430638]
19. Loose M, and Mitchison TJ (2014). The bacterial cell division proteins FtsA and FtsZ self-organize into dynamic cytoskeletal patterns. Nat. Cell Biol. 16, 38–46. [PubMed: 24316672]
20. Yang X, Lyu Z, Miguel A, McQuillen R, Huang KC, and Xiao J (2017). GTPase activity-coupled treadmilling of the bacterial tubulin FtsZ organizes septal cell wall synthesis. Science 355, 744–747. [PubMed: 28209899]

21. Bisson-Filho AW, Hsu YP, Squyres GR, Kuru E, Wu F, Jukes C, Sun Y, Dekker C, Holden S, VanNieuwenhze MS, et al. (2017). Treadmilling by FtsZ filaments drives peptidoglycan synthesis and bacterial cell division. Science 355, 739–743. [PubMed: 28209898]
22. Esue O, Cordero M, Wirtz D, and Tseng Y (2005). The assembly of MreB, a prokaryotic homolog of actin. J. Biol. Chem. 280, 2628–2635. [PubMed: 15548516]
23. Salje J, van den Ent F, de Boer P, and Löwe J (2011). Direct membrane binding by bacterial actin MreB. Mol. Cell 43, 478–487. [PubMed: 21816350]
24. Ozyamak E, Kollman JM, and Komeili A (2013). Bacterial actins and their diversity. Biochemistry 52, 6928–6939. [PubMed: 24015924]
25. Wachi M, Doi M, Tamaki S, Park W, Nakajima-Iijima S, and Matsuhashi M (1987). Mutant isolation and molecular cloning of *mre* genes, which determine cell shape, sensitivity to mecillinam, and amount of penicillin-binding proteins in *Escherichia coli*. J. Bacteriol. 169, 4935–4940. [PubMed: 2822655]
26. Doi M, Wachi M, Ishino F, Tomioka S, Ito M, Sakagami Y, Suzuki A, and Matsuhashi M (1988). Determinations of the DNA sequence of the *mreB* gene and of the gene products of the *mre* region that function in formation of the rod shape of *Escherichia coli* cells. J. Bacteriol. 170, 4619–4624. [PubMed: 3049542]
27. Jones LJF, Carballido-López R, and Errington J (2001). Control of cell shape in bacteria: helical, actin-like filaments in *Bacillus subtilis*. Cell 104, 913–922. [PubMed: 11290328]
28. Kruse T, Bork-Jensen J, and Gerdes K (2005). The morphogenetic MreBCD proteins of *Escherichia coli* form an essential membrane-bound complex. Mol. Microbiol. 55, 78–89. [PubMed: 15612918]
29. van den Ent F, Leaver M, Bendezu F, Errington J, de Boer P, and Löwe J (2006). Dimeric structure of the cell shape protein MreC and its functional implications. Mol. Microbiol. 62, 1631–1642. [PubMed: 17427287]
30. Shiomi D, Sakai M, and Niki H (2008). Determination of bacterial rod shape by a novel cytoskeletal membrane protein. EMBO J. 27, 3081–3091. [PubMed: 19008860]
31. Alyahya SA, Alexander R, Costa T, Henriques AO, Emonet T, and Jacobs-Wagner C (2009). RodZ, a component of the bacterial core morphogenic apparatus. Proc. Natl. Acad. Sci. USA 106, 1239–1244. [PubMed: 19164570]
32. Bendezú FO, and de Boer PA (2008). Conditional lethality, division defects, membrane involution, and endocytosis in *mre* and *mrd* shape mutants of *Escherichia coli*. J. Bacteriol. 190, 1792–1811. [PubMed: 17993535]
33. Mohammadi T, Karczmarek A, Crouvoisier M, Bouhss A, Mengin-Lecreulx D, and den Blaauwen T (2007). The essential peptidoglycan glycosyltransferase MurG forms a complex with proteins involved in lateral envelope growth as well as with proteins involved in cell division in *Escherichia coli*. Mol. Microbiol. 65, 1106–1121. [PubMed: 17640276]
34. Liechti G, Kuru E, Packiam M, Hsu YP, Tekkam S, Hall E, Rittichier JT, VanNieuwenhze M, Brun YV, and Maurelli AT (2016). Pathogenic *Chlamydia* lack a classical sacculus but synthesize a narrow, mid-cell peptidoglycan ring, regulated by MreB, for cell division. PLoS Pathog. 12, e1005590. [PubMed: 27144308]
35. Nguyen LT, Gumbart JC, Beeby M, and Jensen GJ (2015). Coarse-grained simulations of bacterial cell wall growth reveal that local coordination alone can be sufficient to maintain rod shape. Proc. Natl. Acad. Sci. USA 112, E3689–E3698. [PubMed: 26130803]
36. Pinho MG, Kjos M, and Veening J-W (2013). How to get (a)round: mechanisms controlling growth and division of coccoid bacteria. Nat. Rev. Microbiol. 11, 601–614. [PubMed: 23949602]
37. Harris LK, Dye NA, and Theriot JA (2014). A *Caulobacter* MreB mutant with irregular cell shape exhibits compensatory widening to maintain a preferred surface area to volume ratio. Mol. Microbiol. 94, 988–1005.
38. Tsui HT, Boersma MJ, Vella SA, Kocaoglu O, Kuru E, Peceny JK, Carlson EE, VanNieuwenhze MS, Brun YV, Shaw SL, and Winkler ME (2014). Pbp2x localizes separately from Pbp2b and other peptidoglycan synthesis proteins during later stages of cell division of *Streptococcus pneumoniae* D39. Mol. Microbiol. 94, 21–40. [PubMed: 25099088]

39. van Teeffelen S, Wang S, Furchtgott L, Huang KC, Wingreen NS, Shaevitz JW, and Gitai Z (2011). The bacterial actin MreB rotates, and rotation depends on cell-wall assembly. Proc. Natl. Acad. Sci. USA 108, 15822–15827. [PubMed: 21903929]
40. Monteiro JM, Fernandes PB, Vaz F, Pereira AR, Tavares AC, Ferreira MT, Pereira PM, Veiga H, Kuru E, VanNieuwenhze MS, et al. (2015). Cell shape dynamics during the staphylococcal cell cycle. Nat. Commun. 6, 8055. [PubMed: 26278781]
41. Cameron TA, Zupan JR, and Zambryski PC (2015). The essential features and modes of bacterial polar growth. Trends Microbiol. 23, 347–353. [PubMed: 25662291]
42. Liechti GW, Kuru E, Hall E, Kalinda A, Brun YV, VanNieuwenhze M, and Maurelli AT (2014). A new metabolic cell-wall labelling method reveals peptidoglycan in *Chlamydia trachomatis*. Nature 506, 507–510. [PubMed: 24336210]
43. de Boer PAJ (2010). Advances in understanding *E. coli* cell fission. Curr. Opin. Microbiol. 13, 730–737. [PubMed: 20943430]
44. Billings G, Ouzounov N, Ursell T, Desmarais SM, Shaevitz J, Gitai Z, and Huang KC (2014). De novo morphogenesis in L-forms via geometric control of cell growth. Mol. Microbiol. 93, 883–896. [PubMed: 24995493]
45. Kawazura T, Matsumoto K, Kojima K, Kato F, Kanai T, Niki H, and Shiomi D (2017). Exclusion of assembled MreB by anionic phospholipids at cell poles confers cell polarity for bidirectional growth. Mol. Microbiol. 104, 472–486. [PubMed: 28164388]
46. Kim SY, Gitai Z, Kinkhabwala A, Shapiro L, and Moerner WE (2006). Single molecules of the bacterial actin MreB undergo directed treadmilling motion in *Caulobacter crescentus*. Proc. Natl. Acad. Sci. USA 103, 10929–10934. [PubMed: 16829583]
47. Dominguez-Escobar J, Chastanet A, Crevenna AH, Fromion V, Wedlich-Söldner R, and Carballido-López R (2011). Processive movement of MreB-associated cell wall biosynthetic complexes in bacteria. Science 333, 225–228. [PubMed: 21636744]
48. Garner EC, Bernard R, Wang W, Zhuang X, Rudner DZ, and Mitchison T (2011). Coupled, circumferential motions of the cell wall synthesis machinery and MreB filaments in B. subtilis. Science 333, 222–225. [PubMed: 21636745]
49. Fenton AK, and Gerdes K (2013). Direct interaction of FtsZ and MreB is required for septum synthesis and cell division in *Escherichia coli*. EMBO J. 32, 1953–1965. [PubMed: 23756461]
50. Ouzounov N, Nguyen JP, Bratton BP, Jacobowitz D, Gitai Z, and Shaevitz JW (2016). MreB orientation correlates with cell diameter in *Escherichia coli*. Biophys. J. 111, 1035–1043. [PubMed: 27602731]
51. Yao Q, Jewett AI, Chang YW, Oikonomou CM, Beeby M, Iancu CV, Briegel A, Ghosal D, and Jensen GJ (2017). Short FtsZ filaments can drive asymmetric cell envelope constriction at the onset of bacterial cytokinesis. EMBO J. 36, 1577–1589. [PubMed: 28438890]
52. Kuru E, Hughes HV, Brown PJ, Hall E, Tekkam S, Cava F, de Pedro MA, Brun YV, and VanNieuwenhze MS (2012). In situ probing of newly synthesized peptidoglycan in live bacteria with fluorescent D-amino acids. Angew. Chem. Int. Ed. Engl. 51, 12519–12523. [PubMed: 23055266]
53. Ursell TS, Nguyen J, Monds RD, Colavin A, Billings G, Ouzounov N, Gitai Z, Shaevitz JW, and Huang KC (2014). Rod-like bacterial shape is maintained by feedback between cell curvature and cytoskeletal localization. Proc. Natl. Acad. Sci. USA 111, E1025–E1034. [PubMed: 24550515]
54. Strahl H, Bürmann F, and Hamoen LW (2014). The actin homologue MreB organizes the bacterial cell membrane. Nat. Commun. 5, 3442. [PubMed: 24603761]
55. Karczmarek A, Martínez-Arteaga R, Alexeeva S, Hansen FG, Vicente M, Nanninga N, and den Blaauwen T (2007). DNA and origin region segregation are not affected by the transition from rod to sphere after inhibition of Escherichia coli MreB by A22. Mol. Microbiol. 65, 51–63. [PubMed: 17581120]
56. van der Ploeg R, Goudelis ST, and den Blaauwen T (2015). Validation of FRET assay for the screening of growth inhibitors of *Escherichia coli* reveals elongasome assembly dynamics. Int. J. Mol. Sci. 16, 17637–17654. [PubMed: 26263980]

57. Shi H, Colavin A, Bigos M, Tropini C, Monds RD, and Huang KC (2017). Deep phenotypic mapping of bacterial cytoskeletal mutants reveals physiological robustness to cell size. Curr. Biol. 27, 3419–3429.e4. [PubMed: 29103935]
58. Wachi M, and Matsuhashi M (1989). Negative control of cell division by mreB, a gene that functions in determining the rod shape of *Escherichia coli* cells. J. Bacteriol. 171, 3123–3127. [PubMed: 2656641]
59. Takacs CN, Poggio S, Charbon G, Pucheault M, Vollmer W, and Jacobs-Wagner C (2010). MreB drives de novo rod morphogenesis in Caulobacter crescentus via remodeling of the cell wall. J. Bacteriol. 192, 1671–1684. [PubMed: 20023035]
60. Bean GJ, Flickinger ST, Westler WM, McCully ME, Sept D, Weibel DB, and Amann KJ (2009). A22 disrupts the bacterial actin cytoskeleton by directly binding and inducing a low-affinity state in MreB. Biochemistry 48, 4852–4857. [PubMed: 19382805]
61. Szwedziak P, and Löwe J (2013). Do the divisome and elongasome share a common evolutionary past? Curr. Opin. Microbiol. 16, 745–751. [PubMed: 24094808]
62. Sauvage E, Kerff F, Terrak M, Ayala JA, and Charlier P (2008). The penicillin-binding proteins: structure and role in peptidoglycan biosynthesis. FEMS Microbiol. Rev. 32, 234–258. [PubMed: 18266856]
63. Spratt BG (1975). Distinct penicillin binding proteins involved in the division, elongation, and shape of *Escherichia coli K12*. Proc. Natl. Acad. Sci. USA 72, 2999–3003. [PubMed: 1103132]
64. Den Blaauwen T, Aarsman MEG, Vischer NOE, and Nanninga N (2003). Penicillin-binding protein PBP2 of *Escherichia coli* localizes preferentially in the lateral wall and at mid-cell in comparison with the old cell pole. Mol. Microbiol. 47, 539–547. [PubMed: 12519203]
65. Vats P, and Rothfield L (2007). Duplication and segregation of the actin (MreB) cytoskeleton during the prokaryotic cell cycle. Proc. Natl. Acad. Sci. USA 104, 17795–17800. [PubMed: 17978175]
66. Jiang H, Si F, Margolin W, and Sun SX (2011). Mechanical control of bacterial cell shape. Biophys. J. 101, 327–335. [PubMed: 21767484]
67. Swulius MT, and Jensen GJ (2012). The helical MreB cytoskeleton in *Escherichia coli* MC1000/pLE7 is an artifact of the N-terminal yellow fluorescent protein tag. J. Bacteriol. 194, 6382–6386. [PubMed: 22904287]
68. Koppelman C-M, Aarsman MEG, Postmus J, Pas E, Muijsers AO, Scheffers D-J, Nanninga N, and den Blaauwen T (2004). R174 of *Escherichia coli* FtsZ is involved in membrane interaction and protofilament bundling, and is essential for cell division. Mol. Microbiol. 51, 645–657. [PubMed: 14731269]
69. Stiernagle T (2006). Maintenance of *C. elegans*. WormBook, 1–11.
70. Mitchell DH, Stiles JW, Santelli J, and Sanadi DR (1979). Synchronous growth and aging of Caenorhabditis elegans in the presence of fluorodeoxyuridine. J. Gerontol. 34, 28–36. [PubMed: 153363]
71. Petersen JM, Kemper A, Gruber-Vodicka H, Cardini U, van der Geest M, Kleiner M, Bulgheresi S, Mußmann M, Herbold C, Seah BKB, et al. (2016). Chemosynthetic symbionts of marine invertebrate animals are capable of nitrogen fixation. Nat. Microbiol. 2, 16195. [PubMed: 27775707]
72. Meisner J, Montero Llopis P, Sham L-T, Garner E, Bernhardt TG, and Rudner DZ (2013). FtsEX is required for CwlO peptidoglycan hydrolase activity during cell wall elongation in *Bacillus subtilis*. Mol. Microbiol. 89, 1069–1083. [PubMed: 23855774]
73. Vischer NOE, Verheul J, Postma M, van den Berg van Saparoea B, Galli E, Natale P, Gerdes K, Luirink J, Vollmer W, Vicente M, and den Blaauwen T (2015). Cell age dependent concentration of *Escherichia coli* divisome proteins analyzed with ImageJ and ObjectJ. Front. Microbiol. 6, 586. [PubMed: 26124755]
74. Schneider CA, Rasband WS, and Eliceiri KW (2012). NIH Image to ImageJ: 25 years of image analysis. Nat. Methods 9, 671–675. [PubMed: 22930834]

Highlights

- Cell growth is host oriented in an animal symbiont
- Symbiont poles contain bacterial actin homolog MreB and are active growth sites
- The bacterial actin homolog is arranged into a medial ring-like structure
- The bacterial actin homolog is essential for symbiont growth and division

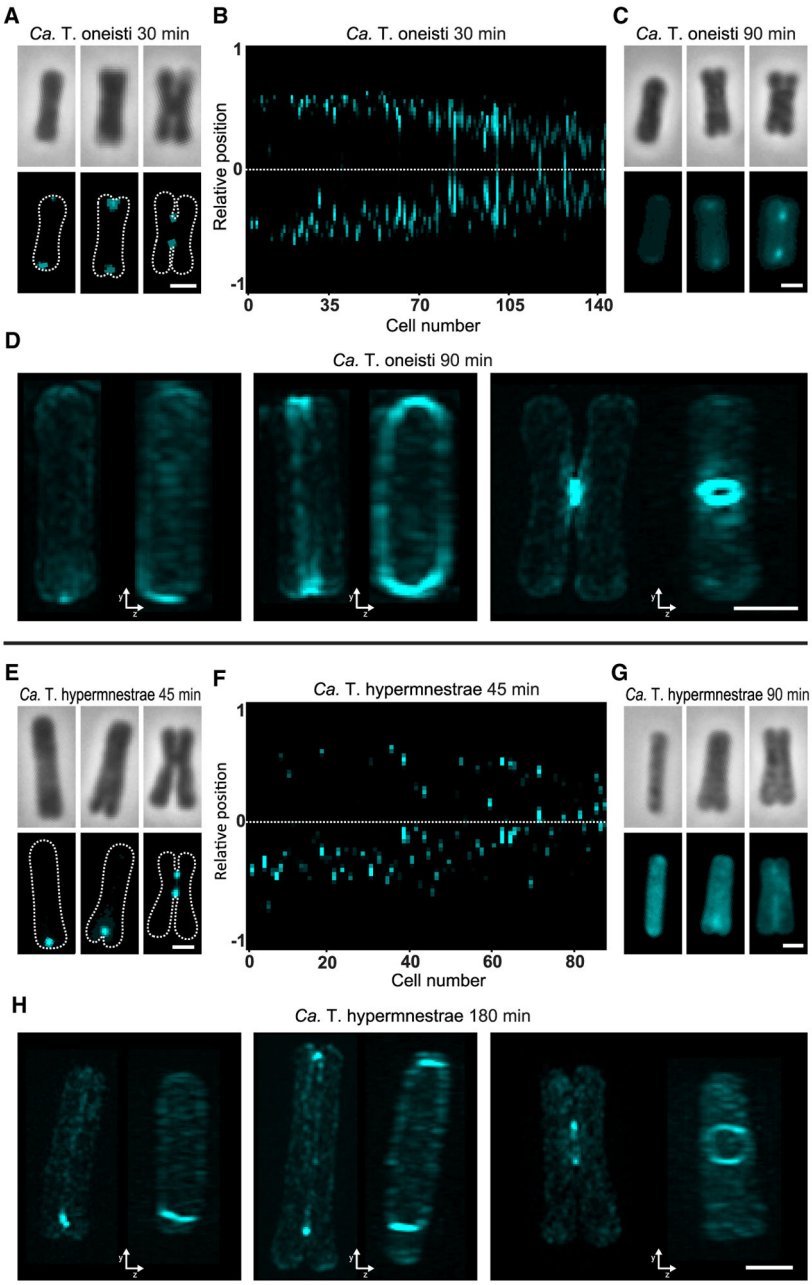

Figure 1. Localization of Newly Synthesized PG in *Ca*. T. oneisti and T. hypermnestrae

(A, C, E, and G) Epifluorescence images of three representative *Ca.* T. oneisti cells (A and C) and of three representative *Ca.* T. hypermnestrae cells (E and G) arranged from the thinnest (youngest) to the thickest (oldest) cell from left to right upon incubation with EDA-DA (incubation length in minutes is specified in each panel). Upper panels show the phase contrast images, and the lower panels show EDA-DA signal (cyan) and cell outlines deduced from the corresponding phase contrast images. The scale bar represents 1 μm. (B and F) Demographs of *Ca.* T. oneisti (B) and *Ca.* T. hypermnestrae (F) cells incubated with 10 Mm EDA-DA(30min and 45min pulse, respectively).The fluorescent EDA-DA signal emitted by each cellwas collapsed into a pixel-wide bar whose length corresponds to the cell long axis

(for *Ca*. T. oneisti length ranges from 2.02 to 3.42 μm and for *Ca*. T. hypermnestrae 2.16–4.29 μm). Symbiont cells were automatically sorted according to increasing width from left to right (i.e., the thinnest cell is on the left end and the widest on the right end of the demograph). In the case of *Ca*. T. hypermnestrae, each bar is oriented such that the upper extremity corresponds to the distal cell pole and the lower extremity corresponds to the proximal pole. Only cells that showedPGincorporation (total cyan fluorescence > 0.01 a.u.) were included in the demographs (25% and 6.4% of the total population for *Ca*. T. oneisti and T. hypermnestrae, respectively). The color intensity corresponds to the integrated amount of EDA-DA fluorescence emitted by each cell. (D and H) Dotted white line indicates the center of the long axis. 3D SIM images of three representative *Ca*. T. oneisti cells incubated with EDA-DA for 90 min (D) and of three *Ca*. T. hypermnestrae cells incubated with EDA-DA for 180 min (H). Cells are ordered from the thinnest (youngest) to thickest (oldest) from left to right. For each cell, a frontal (left) and a 90° shifted side view (right) is shown. The scale bar represents 1 μm. See also Figures S1 and S2.

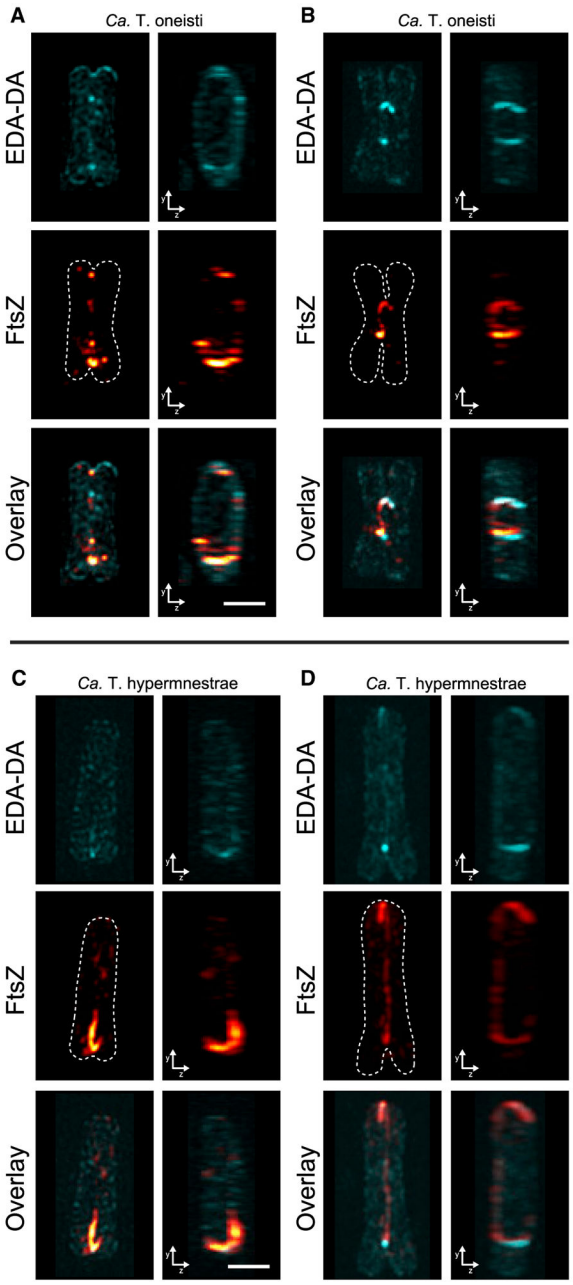

Figure 2. FtsZ Localization Pattern in *Ca*. T. oneisti and T. hypermnestrae Incubated with a PG Metabolic Probe

Two representative *Ca.* T. oneisti cells (A and B) and two representative *Ca.* T. hypermnestrae cells (C and D) incubated with 10 mM EDA-DA (90 min and 180 min, respectively) and immunostained with an FtsZ antibody. Upper panels show EDA-DA signal (cyan), middle panels FtsZ signal (red), and lower panels the corresponding overlay. Dotted white line indicates the cell outline. A frontal view (left) and a corresponding 90° shifted side view (right) is shown for each cell. The scale bar represents 1 μm. See also Movie S1.

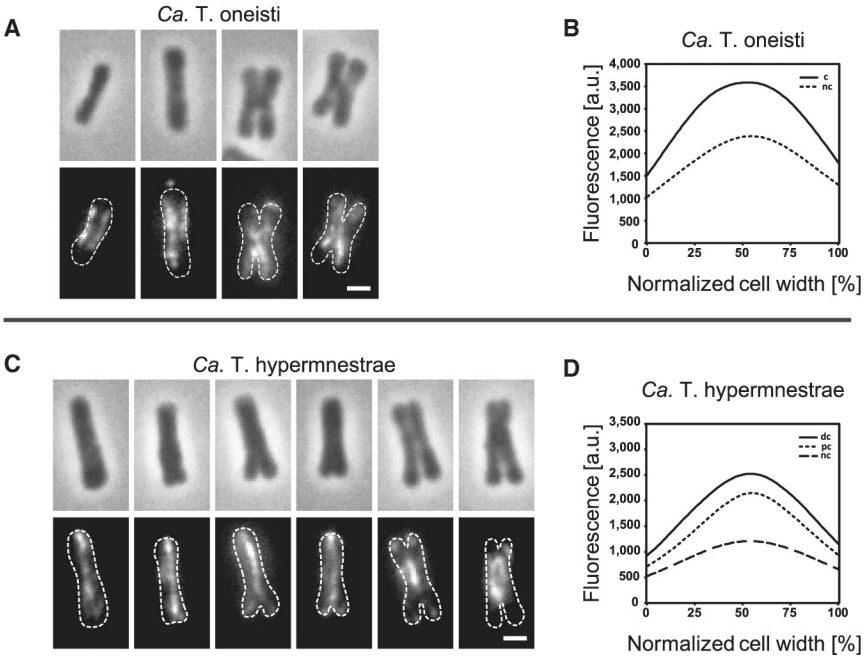

Figure 3. MreB Localization Pattern in *Ca*. T. oneisti and T. hypermnestrae

(A and C) Epifluorescence images of four representative *Ca*. T. oneisti cells (A) and six representative *Ca*. T. hypermnestrae cells (C) immunostained with anti-MreB antibody. For each symbiont, cells are arranged from the youngest to the oldest from left to right. Upper panels display phase contrast images of cells and lower panels their corresponding MreB fluorescence (white dotted line represent cell outlines). The scale bar represents 1 μm. (B and D) Averaged MreB fluorescence (a.u.) plotted against normalized cell width (%) of *Ca*. T. oneisti (B) and *Ca*. T. hypermnestrae (D) cells. In the case of *Ca*. T. oneisti, we plotted the total fluorescence emitted by cells belonging to two morphological classes, non-constricted cells (nc) (dashed line; n = 209) and constricted cells (c) (full line; n = 924). In the case of *Ca*. T. hypermnestrae, we plotted the total fluorescence emitted by cells belonging to three morphological classes, nc (dashed line; n = 973), proximally constricted cells (pc) (dotted line; n = 154), and proximally and distally constricted cells (dc) (full line; n = 155). See also Figures S3, S4, S5, and S6.

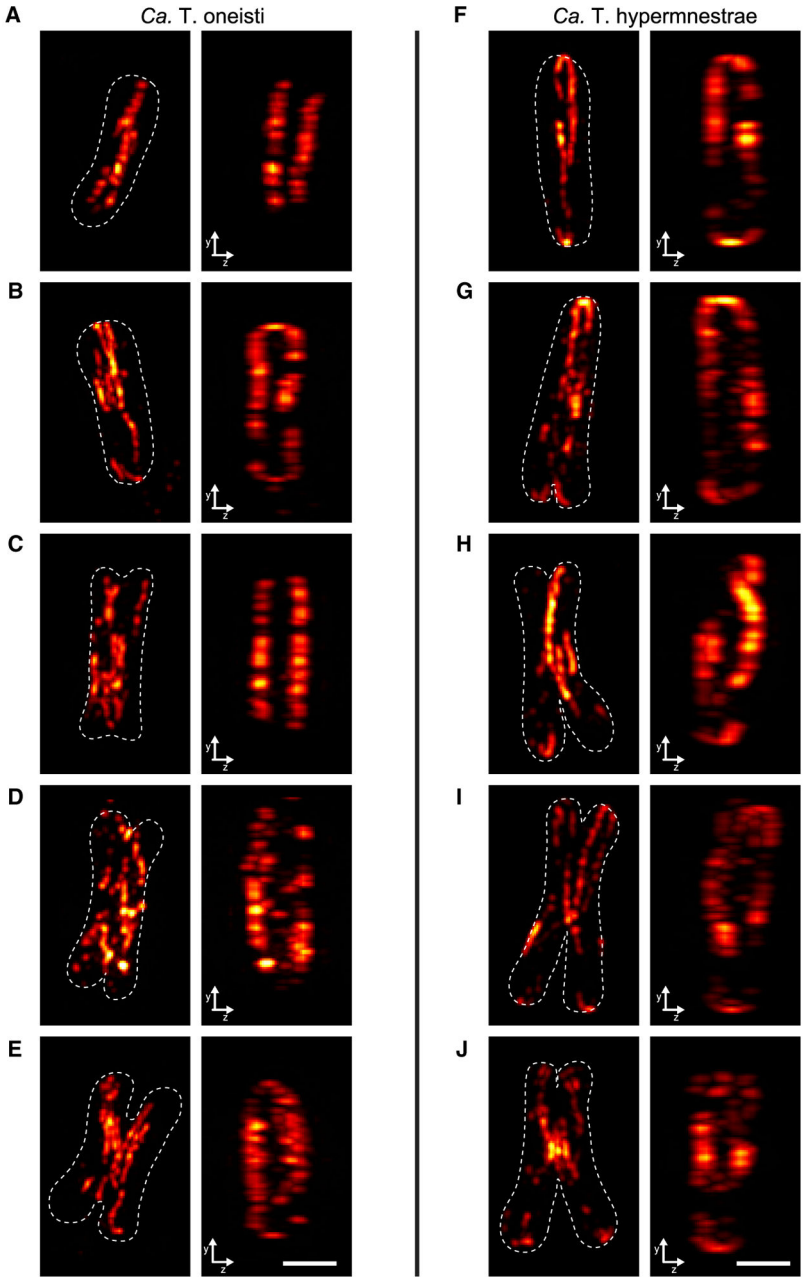

Figure 4. 3D SIM Analysis of MreB Localization Pattern in *Ca*. T. oneisti and T. hypermnestrae

Five representative *Ca*. T. oneisti cells (A–E) and five representative *Ca*. T. hypermnestrae cells (F–J) sorted from the thinnest (top) to the thickest (bottom) immunostained with anti-MreB antibody. Dotted white lines indicate cell outlines. A frontal view (left) and a corresponding 90° shifted side view (right) are shown for each cell. The scale bar represents 1 μm. See also Figures S3 and S5 and Movies S2 and S3.

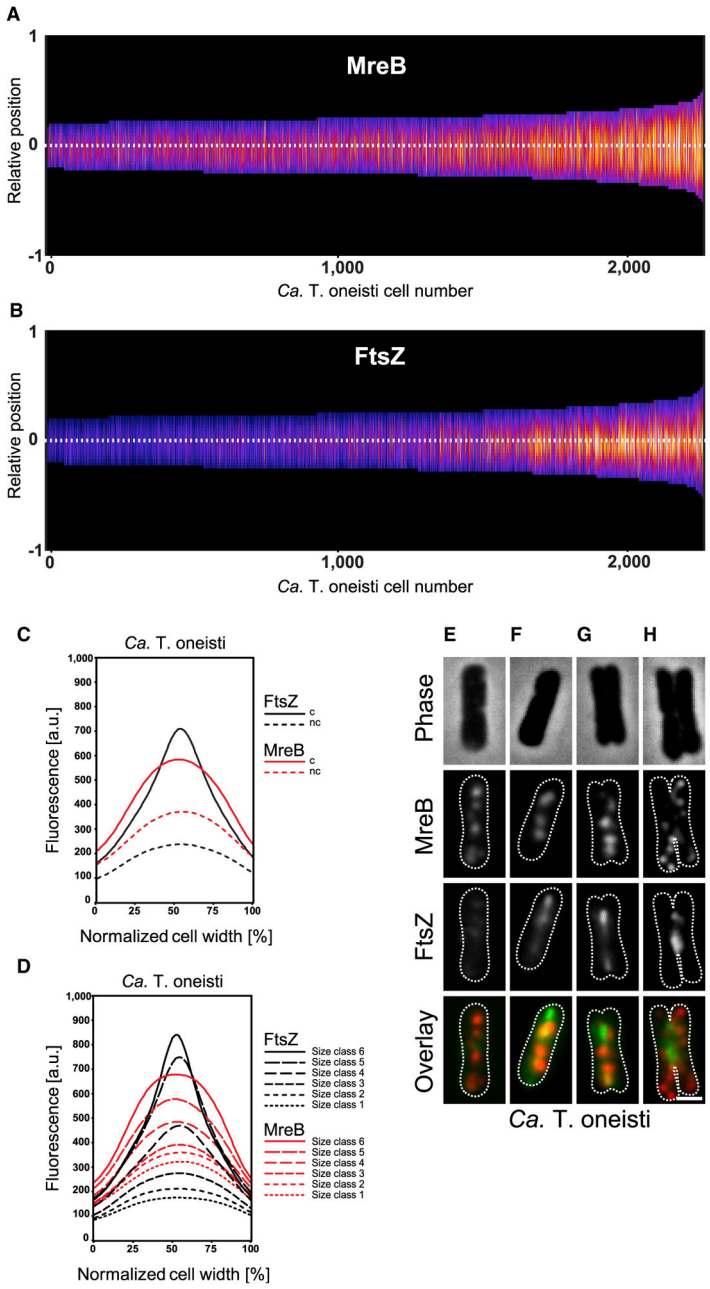

Figure 5. MreB and FtsZ Localization Pattern in *Ca*. T. oneisti

(A and B) Demographs of *Ca.* T. oneisti cells (n = 2,038) immunostained with (A) anti-MreB and (B) anti-FtsZ antibody. Each cell is represented as a pixel-wide bar whose width corresponds to the cell short axis. Symbiont cells were sorted according to increasing width from left to right. Dotted white line indicates the center of the short axis. (C) Average FtsZ and MreB fluorescence (a.u.) plotted against normalized cell width (%) of *Ca.* T. oneisti cells divided into two morphological classes, nc (dashed line; n = 1,594) and c (full line; n = 914). MreB is shown in red and FtsZ in black. (D) Average FtsZ and MreB fluorescence (a.u.) plotted against normalized cell width (%) of *Ca.* T. oneisti cells divided into six width classes (class 1 is 0.53–0.759 μm, n = 462; class 2 is 0.759–0.8376 μm, n = 462; class 3 is

0.8376–0.9246 μm, n = 462; class 4 is 0.9246–1.117 μm, n = 462; class 5 is 1.117–1.295 μm, n = 230; class 6 is 1.295–2.25 μm, n = 230). MreB is shown in red and FtsZ in black. (E–H) Representative non-constricted (E), early septating (F), slightly constricted (G), and deeply constricted (H) *Ca*. T. oneisti cells immunostained with anti-MreB and anti-FtsZ antibodies (red and green in the overlay images, respectively). White dotted lines represent the cell outlines deduced from the corresponding phase contrast images. The scale bar represents 1 μm. See also Figures S3 and S6.

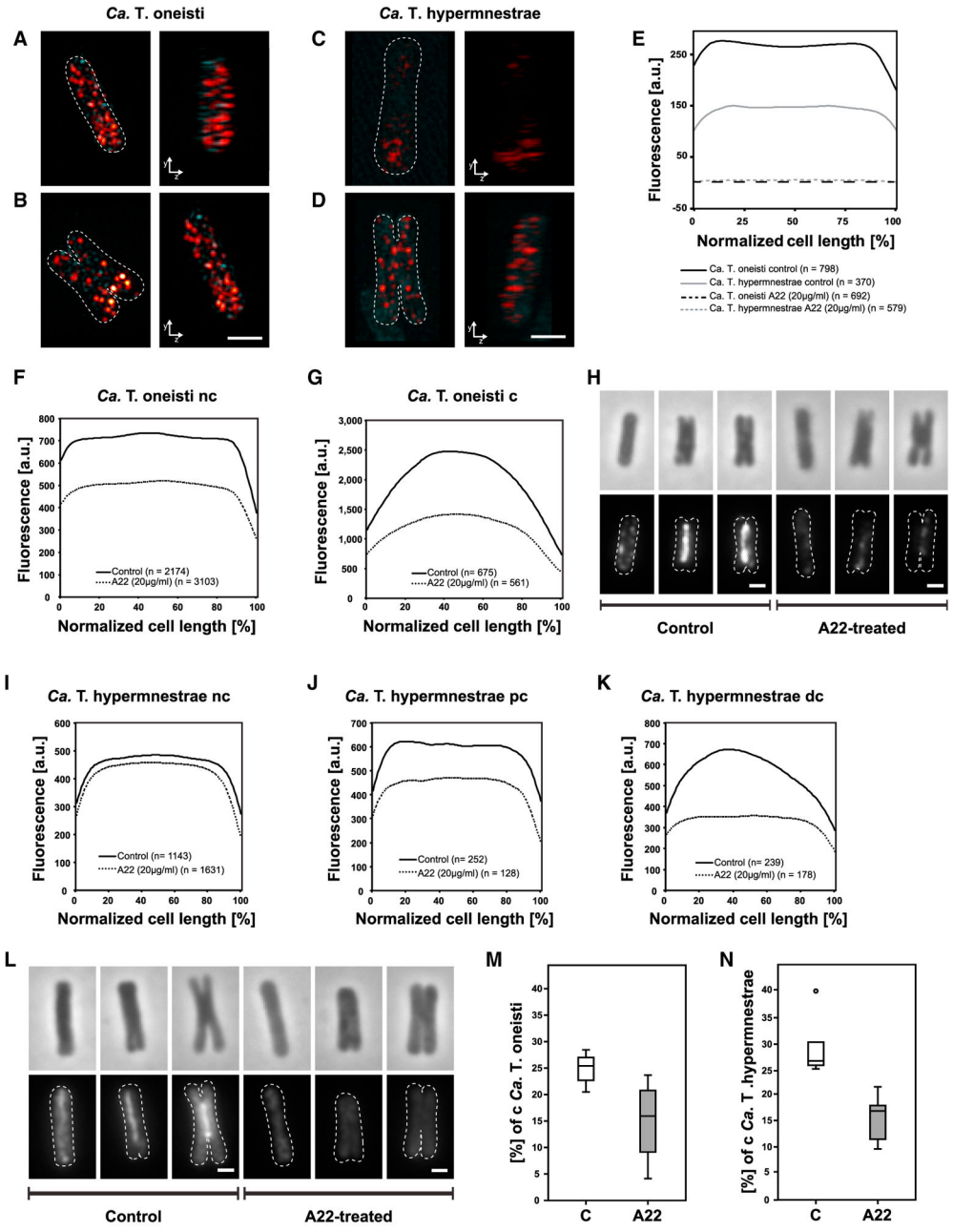

Figure 6. Effect of MreB-Depolymerizing Drug A22 on Ca. T. oneisti and T. hypermnestrae

(A–D) 3D SIM images of a non-constricted (A) and constricted (B) *Ca.* T. oneisti cell and a non-constricted (C) and constricted (D) *Ca.* T. hypermnestrae cell upon A22 treatment. Cells were treated with 20 μg/mL A22 for 120 min prior to addition of 10 mM EDA-DA (cyan; barely detectable). After an additional 90-min-long incubation, cells were fixed, clicked, and immunostained with anti-MreB antibody (red). Dotted white line indicates cell outline. A frontal view (left) and a corresponding 90° shifted side view (right) is shown of each cell. The scale bar represents 1 μm. (E) Averaged EDA-DA fluorescence (a.u.) plotted against normalized cell length (%) of A22-treated (dotted line) and untreated (full line) *Ca.* T. oneisti (black) and *Ca.* T. hypermnestrae (gray) cells. Number of cells is indicated next to

each line. (F and G) Averaged FtsZ fluorescence (a.u.) plotted against normalized cell length (%) of A22-treated and untreated (full line) *Ca*. T. oneisti subdivided into two morphological classes, nc (F) and c (G). n, number of analyzed cells. (H) Phase contrast (top panels) and corresponding epifluorescence images (bottom panels) of representative untreated (left) and A22-treated (right) *Ca*. T. oneisti immunostained with an anti-FtsZ antibody. For each treatment, cells are arranged from the thinnest to the thickest from left to right. White dotted lines represent the cell outlines deduced from the corresponding phase contrast images. The scale bar represents 1 μm. (I–K) Averaged FtsZ fluorescence (a.u.) plotted against normalized cell length (%) of A22-treated and untreated (full line) *Ca*. T. hypermnestrae subdivided into three morphological classes, nc (I), pc (J), and dc (K). (L) Phase contrast (top panels) and corresponding epifluorescence images (bottom panels) of representative untreated (left) and A22-treated (right) *Ca*. T. hypermnestrae immunostained with an anti-FtsZ antibody. For each treatment, cells are arranged from the thinnest to the thickest from left to right. White dotted lines represent the cell outlines deduced from the corresponding phase contrast images. The scale bar represents 1 μm. (M and N) Boxplots showing%of constricted cells in untreated and A22-treated *Ca*. T. oneisti (M) and *Ca*. T. hypermnestrae (N). Symbiont cells were dissociated from 10 untreated and 10 A22-treated *L. oneistus* and from five untreated and A22-treated *R. hypermnestra* nematodes (Tables S3 and S4). Box is the interquartile range (IQR), where the lower edge is 25th percentile (1st quartile [Q1]) and the upper edge the 75th percentile (3rd quartile [Q3]). Whiskers show the range between the lowest value (Min) and the highest value (Max). Line inside each box indicates the median. Black circle in (N) is an outlier. See also Figure S3 and Tables S2, S3, and S4.

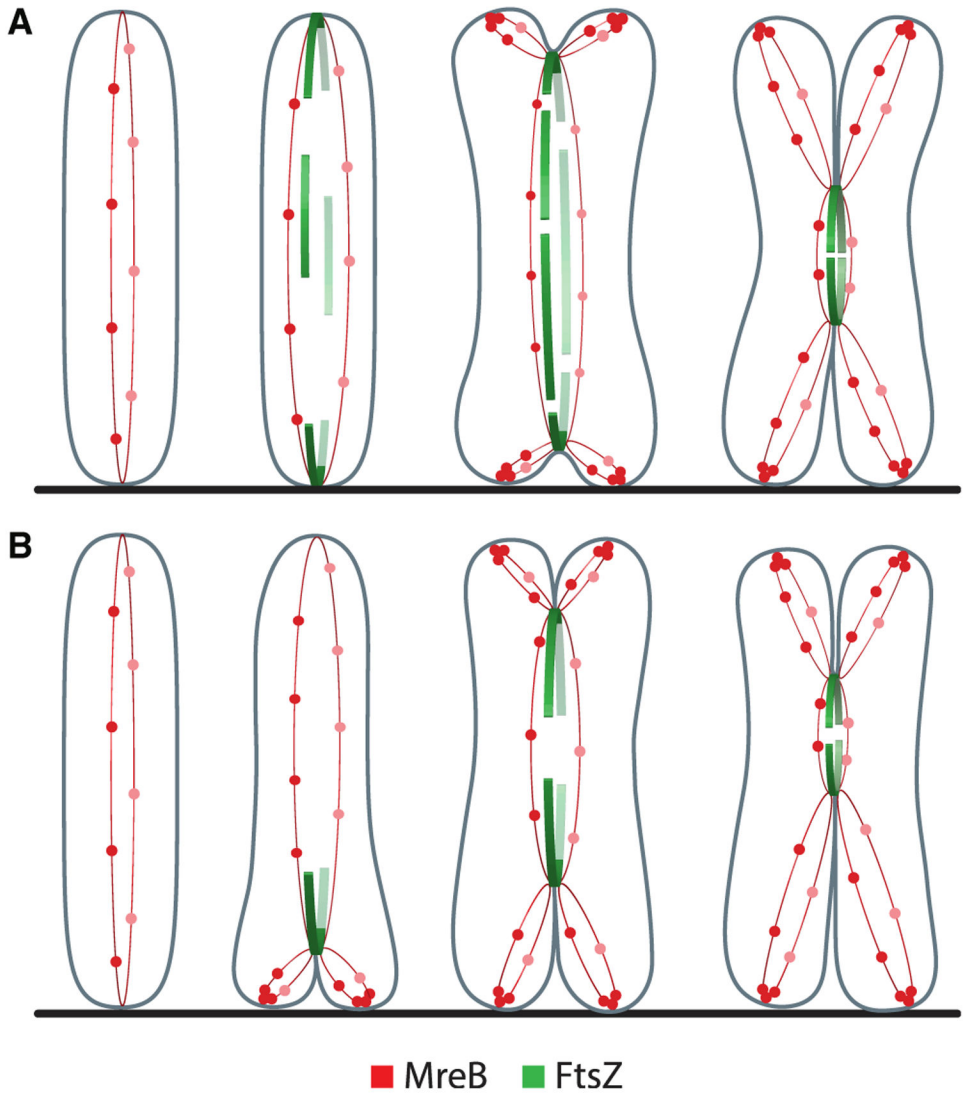

Figure 7. Model of Cell Growth in Longitudinally Dividing Bacteria

Schematic view of MreB and FtsZ localization patterns in *Ca*. T. oneisti (A) and *Ca*. T. hypermnestrae (B). Cells are arranged from the thinnest to the thickest from left to right (see Discussion for explanation).

KEY RESOURCES TABLE

REAGENT or RESOURCE	SOURCE	IDENTIFIER
Antibodies		
Rabbit polyclonal anti-MreB	den Blaauwen, University of Amsterdam [55];	N/A
Rabbit polyclonal anti-FtsZ	den Blaauwen, University of Amsterdam [68];	N/A
Rabbit polyclonal anti-*Ca*. T. oneisti FtsZ	This paper; Genosphere Biotech	N/A
Bacterial and Virus Strains		
Escherichia coli Bl21(DE3) plysS	Invitrogen	Cat#69451
Escherichia coli Dh5α	Widely distributed	N/A
Escherichia coli OP50	Caenorhabditis Genomics Center [69];	N/A
Chemicals, Peptides, and Recombinant Proteins		
Ampicillin	Sigma-Aldrich	Cat#A9518
Chloramphenicol	Sigma-Aldrich	Cat#C0378
A22	Sigma-Aldrich	Cat#SML0471
EDA-DA	VanNieuwenhze, Indiana University Bloomington [34];	N/A
IPTG	Duchefa	Cat#I1401
H-S-MreB	This study	N/A
Critical Commercial Assays		
ÄKTA FPLC Serial #1688191	GE Healthcare	Cat#29018224
HiTrap TALON crude	GE Healthcare	Cat#28953767
Click-iT EdU Alexa Fluor 488 Imaging Kit	Invitrogen	Cat# C10337
Deposited Data		
To*mreB*	This paper	GenBank accession number MF350658
Th*mreB*	This paper	GenBank accession number MF317948

REAGENT or RESOURCE	SOURCE	IDENTIFIER
Experimental Models: Organisms/Strains		
Caenorhabditis elegans N2	Laboratory of Stanley Brul	http://www.wormbase.org/species/c_elegans/strain/N2#02-10
Candidatus Thiosymbion oneisti	Environmental sample collected by the authors for this paper	N/A
Candidatus Thiosymbion hypermnestrae	Environmental sample collected by the authors for this paper	N/A
Oligonucleotides		
pML118-his-sumo-losMreB-fw = 5′-TCACAGAGAACAGATTGGTGGGATGTTTCTCCGACGCATTCG-3′	This paper	N/A
pML118-his-sumo-losMreB-rev = 5′-CTTCCTGCAGTCACCCGGGCCTCCGTCATAGCCAACAGGT-3′	This paper	N/A
pML118-vector-his-sumo-fw = 5′-GCCCGGGTGACTGCAGGAAG-3′	This paper	N/A
pML118-vector-his-sumo-rev = 5′- CCCACCAATCTGTTCTCTGTGA-3′	This paper	N/A
LosRhsMreB_F = 5′- ATGTTTCTCCGACGCATTCGAG-3′	This paper	N/A
LosMreB_R = 5′-CTACTCCGTCATAGCCAACAGGTC-3′	This paper	N/A
RhsMreB_R = 5′- TTACTCGACCACGGTGAACAAATC-3′	This paper	N/A
Recombinant DNA		
Plasmid: pTB146-His-sumo-MreB, see methods details	This paper	N/A
Software and Algorithms		
ImageJ	NIH	https://imagej.nih.gov/ij/
Fiji	ImageJ	https://imagej.net/Fiji
ObjectJ	University of Amsterdam	https://sils.fnwi.uva.nl/bcb/objectj/
SoftWoRx	GE Healthcare Life Sciences	https://www.gelifesciences.com/shop/cell-imaging-and-analysis/high-and-super-resolution-microscopes/instruments/deltavision-omx-p-03478?current=29065721
NIS-Elements AR 4.20.01	Nikon	https://www.nikoninstruments.com/en_EU/Products/Software/NIS-Elements-Advanced-Research
ProgRes Capture Pro 2.8.8	Jenoptik	https://www.jenoptik.com/products/cameras-and-imaging-modules/microscope-cameras/software-solutions/image-software-progres-capture-pro
Photoshop CS6	Adobe Systems	https://www.adobe.com/products/catalog.html
Illustrator CS 6	Adobe Systems	https://www.adobe.com/products/catalog.html
CodonCode Aligner 3.7.1 software	CodonCode Corporation	http://www.codoncode.com/aligner/
SPSS 19.0	SPSS	http://www-01.ibm.com/support/docview.wss?uid=swg24028679